

# Grain Boundary Structure-Property Model Inference Using Polycrystals: The Underdetermined Case

Brandon D. Snow<sup>a</sup>, Sterling G. Baird<sup>a</sup>, Christian Kurniawan<sup>a</sup>, David T. Fullwood<sup>a</sup>, Eric R. Homer<sup>a</sup>,  
Oliver K. Johnson<sup>a,\*</sup>

<sup>a</sup>*Department of Mechanical Engineering, Brigham Young University, Provo, UT 84602, USA*

---

## Abstract

Historically, attempts to correlate grain boundary (GB) structure and properties have relied on experimental measurements and computational calculations performed on bicrystals. While the resulting data can be precise, it is usually severely limited in quantity due to the cost and/or computational expense of sampling the full 5D GB character space. As a result, existing data is concentrated around highly-symmetric sub-regions. In contrast, polycrystals are ubiquitous, inexpensive, and contain a broad range of GB characters. However, extracting GB properties from the effective properties of polycrystals requires the solution of an inverse problem. In this work, we present a Bayesian framework, that we call GB property localization, to address both of these challenges by facilitating the inference of GB structure-property models from indirect polycrystal measurements and severely limited data (i.e. when the system is strongly underdetermined). The method naturally provides uncertainty quantification for the resulting inferences. We present the results of validation tests using 1DOF and 3DOF structure-property models for GB diffusivity in 2D (or columnar) microstructures, and we investigate the influence of the number of observations and the number of grains in a polycrystal on the inference quality. We identify a transition in the preferred type of data as a function of the number of observations: when data is abundant bicrystals lead to more accurate inferences; however when data is severely limited, polycrystals may provide more accurate results.

*Keywords:* Grain Boundary, Structure-Property Model, Inference, Uncertainty Quantification, Inverse Problem

---

## 1. Introduction

Attempts to determine grain boundary (GB) structure-property models have historically relied on experiments or atomistic calculations performed on bicrystals [1–10]. This direct approach gives the researcher high confidence in the measured/calculated properties of a single type of GB, however, the number of direct measurements required to adequately sample the 5D GB character space is rarely available. Rohrer, et al. estimated that to obtain even a  $10^\circ$  resolution (which is quite coarse), a grid over a fundamental zone (FZ) of the 5D GB character space for cubic crystals, would require  $6.5 \times 10^3$  GBs [11]. If the desired resolution decreases to  $5^\circ$  (still coarse, but more useful for property prediction and modeling efforts) the number of required GBs increases to  $2 \times 10^5$  [11]. In contrast, most catalogs of calculated GB properties presently consist of on the order of  $10^2$  GBs [1, 2, 12]. The large number of required measurements/calculations combined with the high cost of those measurements/calculations

---

\*Corresponding author.

*Email address:* ojohnson@byu.edu (Oliver K. Johnson)

suggests that the problem of estimating a 5DOF GB structure-property model is likely to be heavily underdetermined<sup>1</sup> for the foreseeable future, and emphasizes the need for high-throughput measurements/calculations.

One approach to increasing the throughput of measurements is to employ polycrystalline samples. Such samples can include large numbers of GBs, but often only effective, or aggregate, macroscopic properties can be measured, so that resolution of the GB properties requires the solution of an inverse problem.

The work of Bulatov *et al.* [13] is an example of another possible approach to determine a 5DOF structure-property model. In that work, GB energies calculated via molecular dynamics for 388 bicrystals were used to fit 63 parameters of a closed-form geometrical expression or ansatz for GB energy. For many GB properties, however, an appropriate analytical ansatz is not yet known and a non-parametric<sup>2</sup> approach such as the inference method presented here may be preferable. Moreover, if the system is underdetermined, or the available data consists of homogenized effective property measurements from polycrystals an approach such as the one presented in this work may be necessary.

In a companion paper to this work [14] (which we will refer to as [Paper I](#)), we addressed the question: “If I only have access to polycrystals, would it be possible to use them to infer GB structure-property models?” [Paper I](#) answered this question in the affirmative for situations in which the number of measurements exceeds the number of parameters to be inferred (the overdetermined case), and provided methods to solve the necessary inverse problem. However, even using polycrystalline samples, the number of measurements that can be made will be limited, and realistic situations are often likely to be underdetermined.

In this work, the methods of [Paper I](#) are extended to the more challenging underdetermined case, in which we solve the inverse problem of inferring a GB structure-property model from measurements of polycrystal properties, when the number of measurements is far less than the number of model parameters to be inferred. While the focus is specifically on polycrystals, the methods presented here apply also to bicrystal data, if one has access to it, as well as mixtures of polycrystal and bicrystal data.

In the present work we focus on inferring a model for GB diffusivity; however, these inference methods are quite general and apply for any measurable GB property. While we explicitly consider only 2D microstructures with 1DOF and 3DOF structure-property models, the methods presented are applicable to fully 3D microstructures and 5DOF structure-property models.

## 2. Methods

The general approach to solving an underdetermined inverse problem has been well-studied in the field of geostatistics where, *e.g.*, models for sub-surface density distributions are inferred from shock-wave arrival times [15–19]. We will primarily follow methods developed by Tarantola *et al.* [20–26], with necessary adaptations for GBs and the relevant homogenization equations for GB diffusivity in polycrystals.

---

<sup>1</sup>By underdetermined, we mean that the number of data or measurements (knowns) is less than the number of parameters (unknowns) to be inferred.

<sup>2</sup>While the method presented here does indeed involve the use of “parameters” the method is still considered non-parametric for two reasons: (1) the “parameters” result from the use of discretization, which is not an essential element of the method and is used purely for convenience (the method applies for equivalent infinite dimensional functional problems); (2) in contrast to traditional methods that specify an analytical ansatz whose shape is modified by a small number of constants/parameters, the “parameters” in this work simply constitute the values of the inferred function evaluated at an arbitrary large number of specified points.

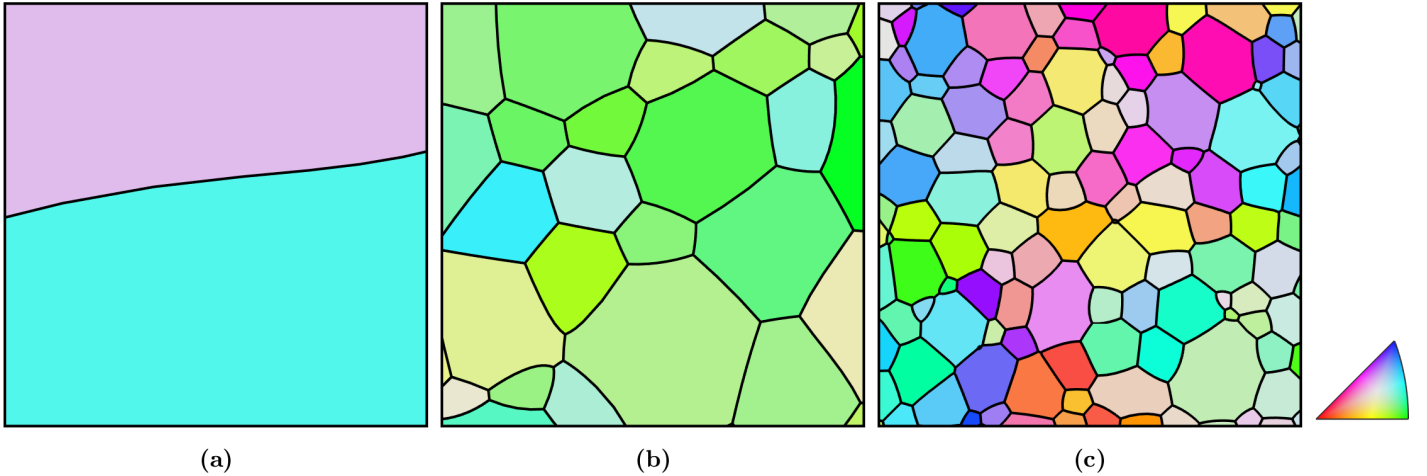


Figure 1: Representative 2D microstructures with (a) 2, (b) 30, and (c) 100 grains, respectively. Grains are colored according to the inverse pole figure (IPF) at right. The diffusion flux is specified to be from left to right and in the plane of the microstructure as shown.

We perform validation testing for the proposed method using simulated microstructures (similar to those generated in [Paper I](#)). Our methods for the creation of a diverse set of microstructures and diffusivity homogenization for GB networks are provided in [Section 2.1](#) and [Section 2.2](#) respectively. In [Section 3](#) we demonstrate the effectiveness of the proposed methods for inferring GB structure-property models and discuss the influence of the number of measurements and polycrystal size on the inference quality.

### 2.1. Microstructures

Two-dimensional microstructures with between 2-100 grains were generated according to the procedure described in [Paper I](#) (see [Fig. 1](#)) using an isotropic, front-tracking, grain growth simulation. The microstructures having fewer than 20 grains were generated by randomly cropping 500 grain microstructures that had themselves been produced by the standard procedure. For each number of grains a separate pool of 1771 microstructures were generated and grain orientations were assigned via a directed Monte Carlo procedure such that each pool of microstructures spanned the majority of the triple junction configuration space [[27–30](#)] (hereafter referred to as the  $J$ -space).

It is worth noting that experimental triple junction fractions typically inhabit a relatively small portion of this space [[31](#)]. Consequently, it is likely that the microstructural diversity presented by these pools of microstructures exceeds that of representative volume elements (RVEs) of typical experimental samples. This may be somewhat ameliorated by the fact that we repeat the inference process multiple times with different randomly selected subsets of microstructures (some of which are highly diverse and others less so), and the quality metrics we report represent the average of these repeated trials. It is also important to acknowledge the significant experimental challenge both of (i) synthesizing and characterizing large numbers of samples (even for polycrystals) and (ii) promoting microstructural diversity. However, it may be possible to enhance the experimentally accessible microstructural diversity in at least two ways.

The first approach involves considering samples that do not constitute an RVE. This will produce samples that have different properties due to statistical fluctuations—cut an RVE into smaller samples and there will be variation in the properties of the sub-samples. Critchfield and Johnson [[32](#)] recently reported RVE sizes for GB networks, which may assist in selecting an appropriately sized sample that balances the desired statistical variability—afforded by having few grains—with ease of fabrication,

handling, and characterization for materials with typical grain sizes. Annealing treatments can also be used to induce intentional grain growth so that large samples (easily handled) with few grains can be fabricated.

A second approach to achieve microstructural diversity experimentally is through variation in processing parameters to produce samples with differing microstructural statistics (crystallographic texture, grain boundary character distribution, etc.). In this case RVEs can be used, but because they were processed differently they will exhibit statistically distinct microstructures with different properties (the properties of two RVEs having different crystallographic textures—e.g. fiber texture vs. random texture—will be distinct even though both are RVEs). Due to practical challenges of producing samples from a wide array of processing routes, we anticipate that the first approach may be easier than the second.

While it is beyond the scope of the present work, we suggest that it would be valuable for future work to investigate the impact of microstructural diversity on inference quality. One additional benefit of such a study may be the implications it might have for optimal experimental designs [33].

## 2.2. Homogenization (The Forward Problem)

A detailed derivation of our homogenization approach for GB network diffusivity is given in [34] and Paper I, so only a brief explanation is provided here. Given a known structure-property model for GB diffusivity,  $\mathcal{D}$ , and the GB network Laplacian,  $\mathcal{L}(M)$ , for the microstructure  $M$ , the effective diffusivity of the GB network can be calculated via

$$\bar{D}^{\text{pred}}(\mathcal{D}, M) = -\frac{L}{A} \mathcal{L}_b^\top \hat{\mathcal{L}}^{-1} e_b \quad (1)$$

where  $L$  is the length of the microstructure in the direction parallel to the flux,  $A$  is the cross-sectional area orthogonal to the flux,  $e_i$  is a vector having the  $i$ -th element equal to 1 and all others equal to 0, and the index  $b$  denotes the “sink” node in the network to which the flux flows. The overbar denotes that this represents the effective diffusivity of the full GB network. We consider conditions for which “Type C” kinetics [35] prevail, where diffusion is limited to the GBs (bulk diffusion is negligible).

To validate our inference approach, we consider two different hypothetical structure-property models for  $\mathcal{D}$  (see Section 3). For each model, we apply Eq. 1 to all observed microstructures,  $\mathbf{M} = \{M_1, M_2, \dots, M_{N_{\text{obs}}}\}$ , to obtain the corresponding homogenized effective diffusivity of the GB network,  $\bar{\mathbf{D}}^{\text{obs}} = \{\bar{D}_1^{\text{obs}}, \bar{D}_2^{\text{obs}}, \dots, \bar{D}_{N_{\text{obs}}}^{\text{obs}}\}$ , where  $\bar{D}_n^{\text{obs}}$  includes noise added according to

$$\ln(\bar{D}^{\text{obs}}) = \ln(\bar{D}^{\text{pred}}) + \epsilon \quad (2)$$

with  $\epsilon \sim \mathcal{N}[0, (\ln(f^2 + 1))^{1/2}]$  and  $f = 0.01$  indicating an assumed noise level of 1%.

The quantities,  $\mathbf{M}$  and  $\bar{\mathbf{D}}^{\text{obs}}$  represent the observed data. The inference problem consists of finding the most probable model given these observations. Validation then consists of comparing the inferred model of  $\mathcal{D}$  to the known model. We note, in passing, that it is also possible to include the uncertainty of  $\mathbf{M}$  due to the finite resolution of the chosen characterization technique (e.g. EBSD), however this uncertainty is negligible compared to the uncertainty in typical measurements of  $\bar{\mathbf{D}}^{\text{obs}}$ , and consequently we do not consider it here.

## 2.3. GB Property Localization (The Inverse Problem)

### 2.3.1. Preliminaries

GB property localization is the inverse problem of inferring a GB structure-property model from measurements. These measurements may be indirect measurements of the macroscopic properties of

polycrystals and/or direct measurements of the properties of individual GBs or bicrystals. The mathematical foundation of GB property localization is based on the conjunction of probability distributions defined on (i) the data space (denoted  $\mathfrak{d}$ ), (ii) the model space (denoted  $\mathfrak{m}$ ), and (iii) the theoretical relationship between the two. The general result is [20]

$$\sigma_m(\mathbf{m}) = k\rho_m(\mathbf{m}) \int_{\mathfrak{d}} \frac{\rho_d(\mathbf{d}) \theta(\mathbf{d} | \mathbf{m})}{\mu_d(\mathbf{d})} d\mathbf{d} \quad (3)$$

where  $\mathbf{m} \in \mathfrak{m}$  and  $\mathbf{d} \in \mathfrak{d}$  denote the set of model and data parameters<sup>3</sup>, respectively;  $\rho_\alpha(\alpha)$  denotes the *a priori* probability density over  $\alpha$  (*i.e.* the prior information we have on  $\alpha$ );  $\theta$  is a conditional distribution that describes the theoretical relationship between  $\mathbf{d}$  and  $\mathbf{m}$ ;  $\mu_\alpha(\alpha)$  is the homogeneous distribution over  $\alpha$ , and  $k$  is a normalization constant. The end result is  $\sigma_m(\mathbf{m})$ , which denotes the *a posteriori* probability density over the model space, quantifying what we know about the model space given our observations and prior information, and represents the most general solution to the inverse problem.

If  $\mathfrak{m}$  and  $\mathfrak{d}$  are linear spaces and the priors are assumed to be Gaussian, then  $\sigma_m(\mathbf{m})$  will also be Gaussian and Eq. 3 takes the particularly simple form [20]

$$\sigma_m(\mathbf{m}) = k \exp\left(-\frac{1}{2}S(\mathbf{m})\right) \quad (4)$$

where

$$S(\mathbf{m}) = (g(\mathbf{m}) - \mathbf{d}_0)^\top \mathbf{C}_{\mathbf{d}_0}^{-1} (g(\mathbf{m}) - \mathbf{d}_0) + (\mathbf{m} - \mathbf{m}_0)^\top \mathbf{C}_{\mathbf{m}_0}^{-1} (\mathbf{m} - \mathbf{m}_0) \quad (5)$$

is referred to as the misfit function. In Eq. 5  $\mathbf{d}_0$  and  $\mathbf{C}_{\mathbf{d}_0}$  are the mean and the covariance operator defining the Gaussian prior on the data space,  $\rho_d(\mathbf{d})$ , and represent the measured data together with their estimated uncertainty. Likewise,  $\mathbf{m}_0$  and  $\mathbf{C}_{\mathbf{m}_0}$  are the mean and the covariance operator defining the Gaussian prior on the model space,  $\rho_m(\mathbf{m})$ , and represent the prior model and its corresponding uncertainty. The functional  $g(\mathbf{m})$  is the non-linear map between the model space and the data space; in materials science parlance we would refer to this functional as a homogenization equation.

While, as mentioned already, the distribution  $\sigma_m(\mathbf{m})$  is itself *the* solution to the inverse problem, one often seeks a single model rather than a distribution over the model space. A natural choice is the model that maximizes the *a posteriori* probability density (often referred to as the maximum *a posteriori* or MAP estimate). Because  $\sigma_m(\mathbf{m})$  is Gaussian, it has a single maximum, corresponding to the minimum of  $S(\mathbf{m})$ , which occurs at [20, 24, 26]

$$\tilde{\mathbf{m}} = \mathbf{m}_0 + \mathbf{C}_{\mathbf{m}_0} \mathbf{G}^* (\mathbf{C}_{\mathbf{d}_0} + \mathbf{G} \mathbf{C}_{\mathbf{m}_0} \mathbf{G}^*)^{-1} (\mathbf{d}_0 - g(\tilde{\mathbf{m}}) + \mathbf{G} (\tilde{\mathbf{m}} - \mathbf{m}_0)) \quad (6)$$

and the *a posteriori* covariance operator is given by [20, 24, 26]

$$\mathbf{C}_{\tilde{\mathbf{m}}} = (\mathbf{I} - \mathbf{C}_{\mathbf{m}_0} \mathbf{G}^* (\mathbf{C}_{\mathbf{d}_0} + \mathbf{G} \mathbf{C}_{\mathbf{m}_0} \mathbf{G}^*)^{-1} \mathbf{G}) \mathbf{C}_{\mathbf{m}_0} \quad (7)$$

where  $(\cdot)^*$  denotes the adjoint of  $(\cdot)$  and  $\mathbf{G}$  is the Fréchet derivative operator, evaluated at  $\tilde{\mathbf{m}}$ . In general, the Fréchet derivative evaluated at a point  $\mathbf{m}$  is defined by [20]

$$\mathbf{G}\delta\mathbf{m} = g(\mathbf{m} + \delta\mathbf{m}) - g(\mathbf{m}) \quad (8)$$

---

<sup>3</sup>The term “parameters” should be understood in an abstract sense. For example,  $\mathbf{m}$  may represent a set, a vector, or, as in the present context a function  $m(\mathbf{x})$ .

where  $\delta \mathbf{m}$  is a small perturbation.

Equation 6 is an implicit equation (note that  $\tilde{\mathbf{m}}$  appears on both the right- and left-hand sides, and that  $\mathbf{G}$  depends on  $\tilde{\mathbf{m}}$ ), and can be solved by an iterative fixed-point method [24]:

$$\tilde{\mathbf{m}}_{k+1} = \mathbf{m}_0 + \mathbf{C}_{\mathbf{m}_0} \mathbf{G}_k^* (\mathbf{C}_{\mathbf{d}_0} + \mathbf{G}_k \mathbf{C}_{\mathbf{m}_0} \mathbf{G}_k^*)^{-1} (\mathbf{d}_0 - g(\tilde{\mathbf{m}}_k) + \mathbf{G}_k (\tilde{\mathbf{m}}_k - \mathbf{m}_0)) \quad (9)$$

where  $\mathbf{G}_k$  denotes the the Fréchet derivative evaluated at  $\tilde{\mathbf{m}}_k$ . The solution is independent of the starting point, but the rate of convergence may be affected by it. As a rule, we choose the prior model  $\mathbf{m}_0$  as the starting point, and convergence typically occurs within a very small number of iterations (often only 3-5). In some of our initial tests we observed an occasional oscillatory behavior of Eq. 9 near the minimum. Consequently, we chose a hybrid approach in which a few iterations of the fixed-point algorithm (Eq. 9) were followed by the following steepest-descent algorithm [20]:

$$\tilde{\mathbf{m}}_{k+1} = \mathbf{m}_k - \mu_k (\mathbf{C}_{\mathbf{m}_0} \mathbf{G}_k^* \mathbf{C}_{\mathbf{d}_0}^{-1} (g(\tilde{\mathbf{m}}_k) - \mathbf{d}_0) + (\tilde{\mathbf{m}}_k - \mathbf{m}_0)) \quad (10)$$

where  $\mu_k$  is a step size that can be optimized to minimize the misfit along the direction of steepest descent. This hybrid approach combines the quick convergence of Eq. 9 along with the smooth behavior of Eq. 10.

### 2.3.2. Problem-Specific Considerations

For the present problem of inferring a structure-property model for GB diffusivity, we define each of the quantities mentioned in Section 2.3.1 as follows<sup>4</sup>

$$\mathbf{m} = \ln(\mathcal{D}) \quad (11)$$

$$\mathbf{d}_0 = \ln(\bar{\mathbf{D}}^{\text{obs}}) \quad (12)$$

$$\begin{aligned} g(\mathbf{m}) &= \ln(\bar{D}^{\text{pred}}(\mathcal{D}, M)) \\ &= \ln(\bar{D}^{\text{pred}}(e^{\mathbf{m}}, M)) \end{aligned} \quad (13)$$

The logarithmic transformations employed permit the definition of Gaussian distributions since  $\mathbf{m}, \mathbf{d}, g(\mathbf{m}) \in (-\infty, \infty)$ , whereas (under most circumstances)  $\mathcal{D}, \bar{D}^{\text{obs}}, \bar{D}^{\text{pred}}(\mathcal{D}, M) \in [0, \infty)$ , which would not be consistent with the domain of a Gaussian distribution. It is straightforward to verify that with these definitions  $\mathbf{m} \in \mathfrak{m}$  and  $\mathbf{d} \in \mathfrak{d}$  are linear spaces. It is not obvious, however, that  $g(\mathbf{m})$  is linear.

Strict linearity is not required for the simplifications leading to Eq. 4 to hold. As long as  $g(\mathbf{m})$  is “not too non-linear” (and this is a rather flexible constraint) then  $\sigma_m(\mathbf{m})$  will still be approximately Gaussian. To verify that  $g(\mathbf{m})$  is “not too non-linear”, we performed numerical tests in which two models,  $\mathbf{m}_A$  and  $\mathbf{m}_B$ , were introduced into Eq. 13 and we compared  $g(\mathbf{m}_A + \mathbf{m}_B)$  to  $g(\mathbf{m}_A) + g(\mathbf{m}_B)$  with a variety of test functions having contrast ratios spanning many orders of magnitude. Figure 2 illustrates that  $g(\mathbf{m})$  is approximately affine-linear, meaning that  $g(\mathbf{m}_A + \mathbf{m}_B) \propto g(\mathbf{m}_A) + g(\mathbf{m}_B)$ . Evidence that this constitutes sufficiently linearity is furnished by the successful validation results presented in Section 3.

There are a variety of possible choices for the covariance operators in Eq. 5. For the data covariance we use

$$\mathbf{C}_{\mathbf{d}_0} : (\ln(f^2 + 1)) \delta_{ij} \quad (14)$$

where  $f = 0.01$ , and as is apparent from this definition,  $\mathbf{C}_{\mathbf{d}_0}$  is a discrete linear operator due to the fact that we have a discrete set of observations.

---

<sup>4</sup>Any reference to the logarithm of diffusivity implicitly assumes a prior division by  $1 \text{ m}^2/\text{s}$  so that the argument to the logarithm is unitless. Correspondingly, when the quantity  $\mathbf{m}$  is exponentiated, the result is implicitly multiplied by  $1 \text{ m}^2/\text{s}$  to obtain the correct units for diffusivity.

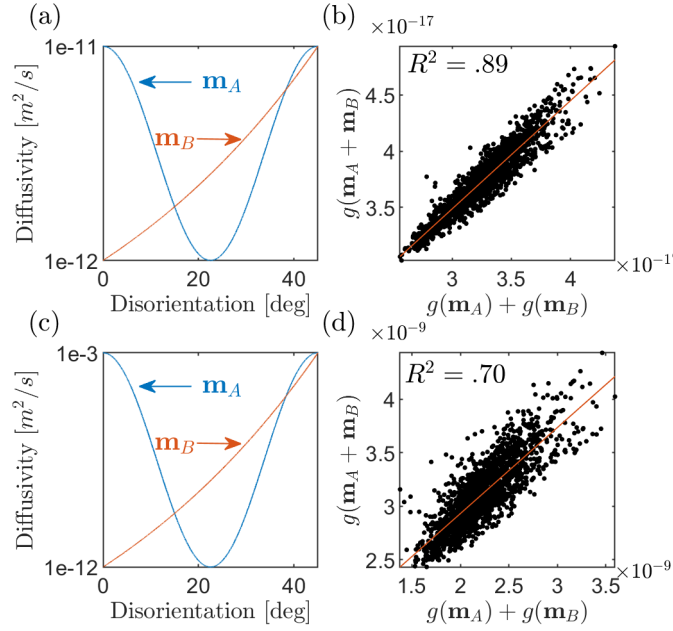


Figure 2: The effect of property contrast on the linearity of the homogenization equation. For (a) & (b) the test functions span 1 order of magnitude (a contrast ratio of 10). For (c) & (d) a contrast ratio of  $10^9$  is employed. The functional  $g(\mathbf{m})$  is linear in  $\mathbf{m}$  if  $g(\mathbf{m}_A + \mathbf{m}_B) = g(\mathbf{m}_A) + g(\mathbf{m}_B)$ . The results in (b) and (d) suggest that the homogenization equation used, while not exactly linear, is approximately affine-linear, and that this holds across a broad range of contrast ratios. In addition to the exponential and cosine functions used in this example, other models for  $\mathbf{m}_A$  and  $\mathbf{m}_B$  were tested and the results were essentially unchanged.

For the model covariance function, we select a Gaussian covariance operator of the form

$$\mathbf{C}_{\mathbf{m}_0} : C_{\mathbf{m}_0}(\mathbf{x}, \mathbf{x}') = \sigma_{\mathbf{m}_0}^2 \exp\left(-\frac{d^2(\mathbf{x}, \mathbf{x}')}{2\ell^2}\right) \quad (15)$$

where  $\mathbf{x}$  and  $\mathbf{x}'$  are two points in the domain of  $\mathbf{m}$  (the GB character space, or a subspace of it);  $\sigma_{\mathbf{m}_0}$  is the standard deviation (a scalar constant and the chosen measure of model uncertainty)<sup>5</sup>;  $\ell$  is a length-scale over which we expect the function  $\mathbf{m}$  to be smooth (for the present work<sup>6</sup> we choose a value of  $5^\circ$ ); and  $d^2(\mathbf{x}, \mathbf{x}')$  is the squared distance between points  $\mathbf{x}$  and  $\mathbf{x}'$ . The model covariance function (Eq. 15) encodes the soft constraint from our prior knowledge that GBs that are crystallographically similar (as defined by their distance,  $d^2(\mathbf{x}, \mathbf{x}')$ , relative to the length scale  $\ell$ ) should have similar properties.

In this work, we consider 1DOF GB structure-property models, in which the GB diffusivity is a function of only the disorientation angle  $\mathcal{D}(\omega)$ , as well as 3DOF GB structure-property models, in which the GB diffusivity is a function of all three disorientation parameters  $\mathcal{D}(\omega, \theta, \phi)$  with  $\theta$  and  $\phi$  defining the polar and azimuthal angles of the disorientation axis. For the 1D structure property model  $\mathbf{x} \equiv \omega$ , and the covariance operator defined in Eq. 15 is positive definite, which is required for the

<sup>5</sup>not to be confused with the posterior distribution  $\sigma_m(\mathbf{m})$

<sup>6</sup>It is common in Bayesian inference problems to perform hyper-parameter optimization to select values for parameters like  $\ell$ . However, caution should be taken to prevent over-fitting on limited data with non-physical parameter values. For example, on tests with sparse data, hyper-parameter optimization produced “optimal” values of  $\ell$  as large as  $45^\circ$  or more, which would impose artificially strong correlations between very dissimilar GBs. We suggest that when physical intuition is available to inform the choice of  $\ell$  it is preferable to unsupervised hyper-parameter optimization.

resolution of the inverse problem.

However, for the 3DOF case  $\mathbf{x} \equiv \mathbf{q}(\omega, \theta, \phi)$  is the quaternion representing the disorientation (using an active rotation convention) and  $d^2(\mathbf{x}, \mathbf{x}')$  is the squared distance between two disorientations, which we take as the square of the minimum rotation angle between two disorientations among all symmetrically equivalent pairs of misorientations:

$$d(\mathbf{q}, \mathbf{q}') = \min_{\substack{i,j,k \\ l,m,n}} 2 \arccos\left(\left(\mathbf{s}_j^{-1} \mathbf{q}_i \mathbf{s}_k\right)^{-1} \left(\mathbf{s}_m^{-1} \mathbf{q}'_l \mathbf{s}_n\right)\right) \quad (16)$$

where  $\mathbf{s}_a$  is the quaternion representation of the  $a$ -th symmetry operator of the corresponding disorientation, and  $\mathbf{q}_i \in \{\mathbf{q}, \mathbf{q}^{-1}\}$  and  $\mathbf{q}'_l \in \{\mathbf{q}', (\mathbf{q}')^{-1}\}$  also include grain-exchange symmetry [36] for each of the disorientations. This distance metric is not Euclidean and consequently the corresponding covariance operator,  $C_{\mathbf{m}}(\mathbf{q}, \mathbf{q}')$ , is not guaranteed to be positive definite [37]. This problem arises in many fields when covariance operators are defined using non-Euclidean distance metrics [37], and a variety of solutions have been proposed. We employ the program `nearestSPD` [38], which uses Higham’s method [39] of finding the unique nearest symmetric positive semi-definite matrix (in the Frobenius norm) and then adding a small perturbation of the form  $\epsilon \mathbf{I}$ , where  $\epsilon$  is some small positive constant.

### 2.3.3. Uncertainty Quantification

One of the advantages of this probabilistic framework is that uncertainty quantification is a natural result of the process. The uncertainty in the MAP estimate of the GB structure-property model is quantitatively described by the posterior covariance operator,  $C_{\mathbf{m}}$ , defined in Eq. 7. To present this in a way that is familiar, we extract the standard deviation of  $m(\mathbf{x})$  at each point  $\mathbf{x}$  from the posterior covariance operator according to

$$\sigma_{\mathbf{m}}(\mathbf{x}) = \sqrt{C_{\mathbf{m}}(\mathbf{x}, \mathbf{x})} \quad (17)$$

The inferred model can then be presented with typical error bars showing one standard deviation as defined by  $m(\mathbf{x}) \pm \sigma_{\mathbf{m}}(\mathbf{x})$ . Remembering that  $m(\mathbf{x})$  represents the log-transformation of  $\mathcal{D}(\mathbf{x})$ , we can rewrite the uncertainty interval lower and upper limits as

$$\exp(m(\mathbf{x}) - \sigma_{\mathbf{m}}(\mathbf{x})) = \exp(m(\mathbf{x})) / \exp(\sigma_{\mathbf{m}}(\mathbf{x})) \quad (18)$$

$$\exp(m(\mathbf{x}) + \sigma_{\mathbf{m}}(\mathbf{x})) = \exp(m(\mathbf{x})) \exp(\sigma_{\mathbf{m}}(\mathbf{x})) \quad (19)$$

And recognizing

$$\mathcal{D}(\mathbf{x}) = \exp(m(\mathbf{x})) \quad (20)$$

$$\sigma_{\mathcal{D}}(\mathbf{x}) = \exp(\sigma_{\mathbf{m}}(\mathbf{x})) \quad (21)$$

the uncertainty scatter interval for  $\mathcal{D}(\mathbf{x})$  can be expressed compactly as  $\mathcal{D}(\mathbf{x}) * \sigma_{\mathcal{D}}(\mathbf{x})$ , where  $*$  indicates “multiply-or-divide” instead of “plus-or-minus”. This means that when the uncertainty in the inferred model is expressed in terms of  $\sigma_{\mathcal{D}}(\mathbf{x})$  one should remember that it is multiplicative, *not* additive.

### 2.3.4. Validation

As the objective of this work is to evaluate the potential of the proposed method of inferring GB structure-property models when only limited and possibly indirect data is available, we use several methods to evaluate the quality of the inferred models. Two of these (misfit and resolving power) are general and will be applicable to actual inferences performed when the true model is not known, and one (median absolute error) is specific to this validation study and involves comparison of the inference to the true model. We define each of these here.

The misfit has already been defined in Eq. 5. Note that from the Bayesian viewpoint, the function  $\mathbf{m}$  is considered a random variable. Consequently, the value of the misfit function at the MAP point,  $S(\tilde{\mathbf{m}})$ , is also a random variable, and, for linear inverse problems,  $S(\tilde{\mathbf{m}})$  is distributed according to a  $\chi^2$  distribution with the same number of degrees of freedom as there are observations,  $N_{\text{obs}}$  [20]. For inverse problems that are approximately linear, this is still approximately true. Since the expected value of a  $\chi^2$  distribution with  $N_{\text{obs}}$  degrees of freedom is  $N_{\text{obs}}$ , this furnishes us with a way to evaluate the quality of the inference: the misfit of the inferred model should be close to  $N_{\text{obs}}$ . Hence, when plotting results that compare inferences using different number of observations (Figs. 5 and 8), we will normalize the value of the misfit function by  $N_{\text{obs}}$ , so that inferences with a normalized misfit near unity are expected regardless of the number of observations. This should be understood as a rough way to evaluate both the degree to which the inference result is consistent with the observations and prior assumptions, and how well the inference process has converged. Extremely large deviations from this expected value would suggest a possible inconsistency in the *a priori* assumptions (e.g. Gaussian priors) or an overestimation of prior uncertainties [20].

We define *resolving power* as the relative reduction in uncertainty when comparing the posterior distribution to the prior distribution over  $\mathbf{m}$ . This is a measure of the amount of information learned by the inference process, or how much the data has enabled us to resolve the inverse problem. Mathematically, we can express this as

$$RP = \frac{\int_{\mathbf{x}} \sigma_{\mathbf{m}}^2(\mathbf{x}) - \sigma_{\mathbf{m}_0}^2(\mathbf{x}) d\mathbf{x}}{\int_{\mathbf{x}} \sigma_{\mathbf{m}_0}^2(\mathbf{x}) d\mathbf{x}} \quad (22)$$

The resolving power is 0 if the uncertainty is unchanged during the inference, and 1 if the posterior model has 0 uncertainty. For practical computations we replace the integral with a finite summation of the discretized values

$$RP \approx \frac{\sum_i \sigma_{\mathbf{m}}^2(\mathbf{x}_i) - \sigma_{\mathbf{m}_0}^2(\mathbf{x}_i)}{\sum_j \sigma_{\mathbf{m}_0}^2(\mathbf{x}_j)} \quad (23)$$

To compare the inferred models to the true model, we employ the median absolute error

$$\text{MedAE} = \text{median}(|\tilde{\mathbf{m}} - \mathbf{m}_{\text{true}}|) \quad (24)$$

This provides a measure of the average prediction error using the inferred model.

### 3. Results & Discussion

The 1DOF and 3DOF models employed to validate our inference approach are shown in Fig. 3. Both models exhibit cusps, which are anticipated to be characteristic features of any GB structure-property model (see e.g. [13]). During the 2D microstructure generation described in Section 2.1, cubic crystal symmetry was assumed. Microstructures intended to be used with the 1DOF model had grain orientations assigned all sharing a common [100] rotation axis. Consequently, GB disorientation angles for this model inhabit  $\omega \in [0^\circ, 45^\circ]$  as is apparent from the domain of Fig. 3(a). Microstructures intended for use with the 3DOF model had grain orientations assigned from the full cubic orientation FZ, so that the possible GB disorientations inhabit the full cubic misorientation FZ shown in Fig. 3(b).

For each inference, the prior model (or initial guess),  $\mathbf{m}_0$  was chosen to be a constant with a value in the middle of the expected range of values (such might be a reasonable estimate based on existing measurements or literature values of single-crystal and “general” GB properties), and the uncertainty,  $\sigma_{\mathbf{m}_0}$ , was set to half this range (see Fig. 4).

Many inferences were performed to determine the influence of the number of grains,  $N_{\text{grains}}$ , and the number of observations,  $N_{\text{obs}}$ , on the quality of the inference. In preliminary testing we observed

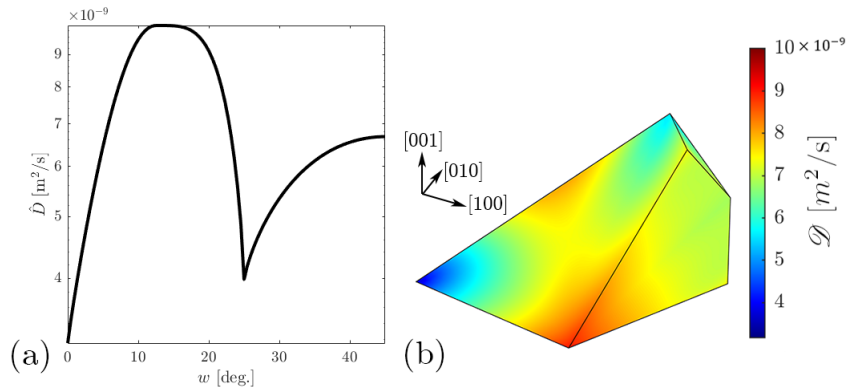


Figure 3: “True” diffusivity models that were used to test the inference method. (a) shows the 1DOF model based solely on the disorientation angle  $\omega$  and (b) shows a 3DOF model based on the disorientation angle and axis (represented here in the cubic misorientation FZ in Rodriguez space).

for  $N_{\text{grains}} \gtrsim 100$  several quantities became nearly independent of  $N_{\text{grains}}$ . For example, in 1DOF inferences with 10 observations, microstructures with 1000 grains—which approach the size of the GB network RVEs computed in [32]—had median absolute errors of  $0.095 \pm 0.024$ , compared to the 100 grain microstructures reported here that exhibited median absolute errors of  $0.094 \pm 0.039$ . Nevertheless, in some situations dependence on  $N_{\text{grains}}$  was observed for even higher values. In an effort to balance observation of important trends with computational efficiency, we present inference results for  $N_{\text{grains}} \in [2, 100]$ , in steps of 1 for  $N_{\text{grains}} \leq 19$  and steps of 10 for  $N_{\text{grains}} \geq 20$ . For the 1DOF case we considered  $N_{\text{obs}} \in [2, 100]$  (any more observations would make the system overdetermined), and for the 3DOF case we considered  $N_{\text{obs}} \in [2, 300]$ . For each inference  $N_{\text{grains}}$  was first fixed and then a subset of microstructures was chosen uniformly at random from the candidate pool of 1771 microstructures (described in Section 2.1) for that number of grains. This process was repeated 10 times and the median value of each of the quality metrics across the 10 replications for every combination of  $N_{\text{grains}}$  and  $N_{\text{obs}}$  is reported. Figure 5 and Figure 8 show results for all tested combinations.

### 3.1. 1DOF Results

For the 1DOF inferences, the disorientation angle domain of  $\omega \in [0^\circ, 45^\circ]$  was discretized into 100 points, so that the model parameters to be inferred consisted of the logarithm of the function values at each of these points:  $\mathbf{m} = \ln([\mathcal{D}(\omega_1), \mathcal{D}(\omega_2), \dots]^\top)$ . A few representative inferences are shown in (Fig. 4).

As expected the quality of inferences increases with  $N_{\text{obs}}$  (compare e.g. Fig. 4(a) and (c)). This trend is reproduced over the full set of test conditions shown in Fig. 5(b). However, Fig. 4 also illustrates important differences between the inference results produced by bicrystal data and polycrystal data (i.e. the effect of  $N_{\text{grains}}$ ).

In Fig. 4(a) the posterior estimate is accurate and the posterior uncertainty is dramatically reduced only in the vicinity of the 5 bicrystal observations. Away from these points (e.g.  $\omega \lesssim 5^\circ$ ) the posterior estimate and uncertainty are indistinguishable from the priors. In contrast, with the same number of polycrystal observations Fig. 4(b) shows improved estimates and reduced uncertainty across the entire domain. This suggests that, for the same number of observations, with bicrystal data we learn a lot about a small region of the space, whereas with polycrystal data what we learn is spread over a more diffuse region.

For a 1DOF structure-property model, one could remedy the highly localized knowledge of bicrystals by means of a regular (as opposed to random) sampling strategy, evenly spacing bicrystals across the

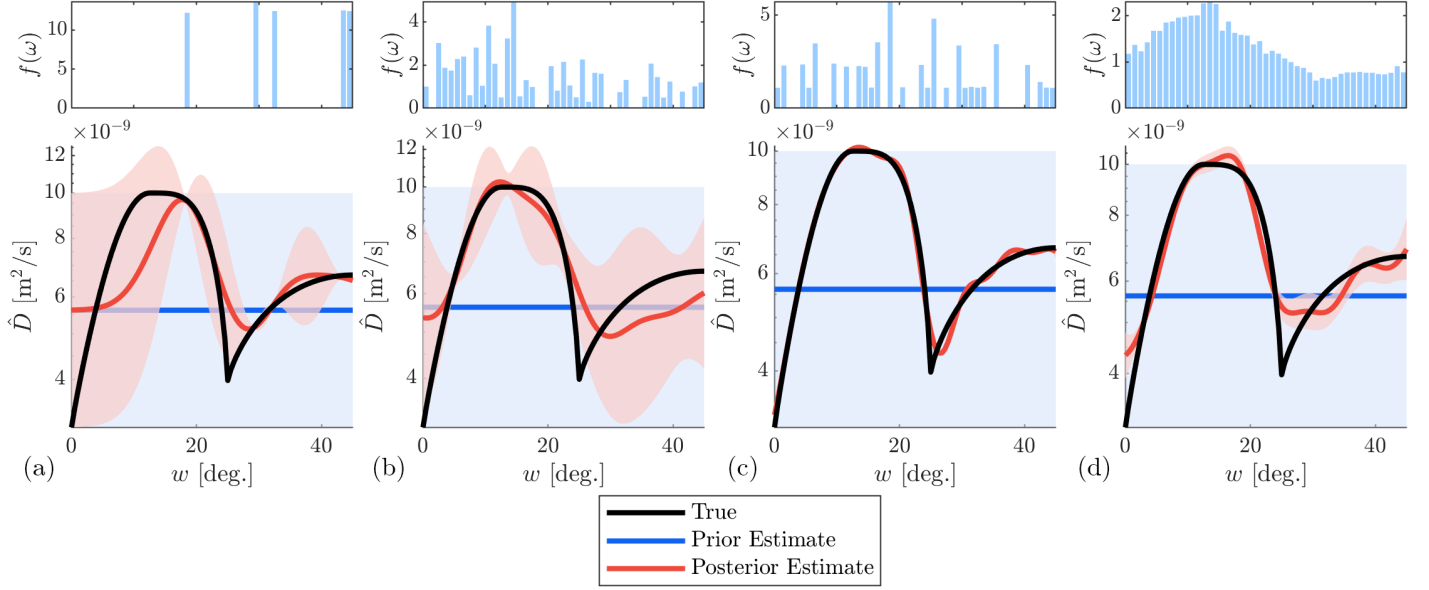


Figure 4: Four representative inferences, A, B, C & D which correspond to the A,B,C & D labels on Fig. 5. The four examples are the inferences that result from A: 5 bicrystal observations, B: 5 polycrystal (10 Grain) observations, C: 50 bicrystal observations, and D: 50 large polycrystal (100 Grain) observations. The histograms above each plot represent the distribution (probability density) of GBs present in each pool of observations.

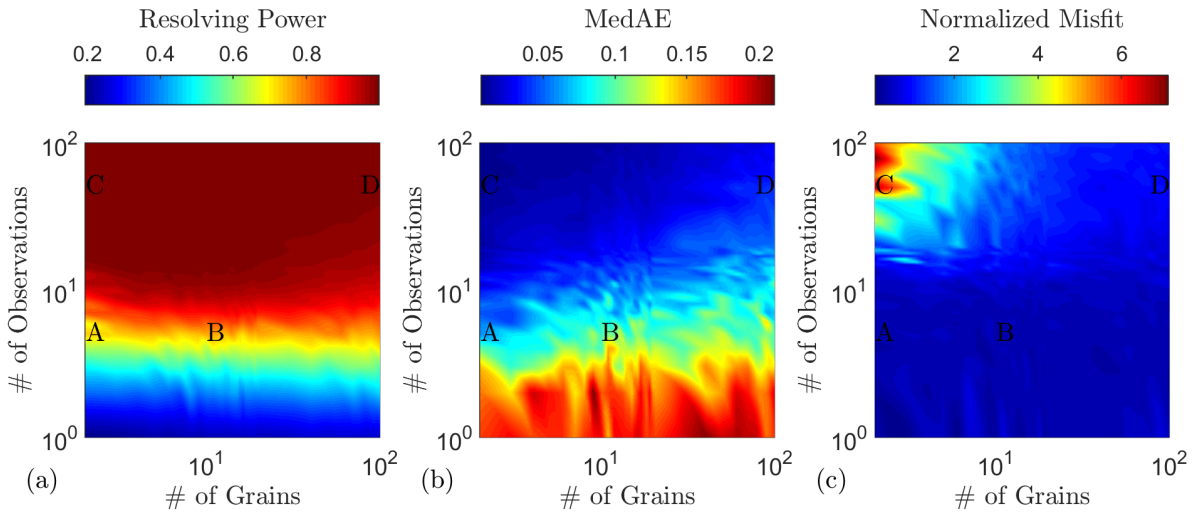


Figure 5: Contour plots of (a) resolving power (see Eq. 23), (b) median absolute error (see Eq. 24) between the inference and the true model, and (c) the normalized misfit of the inferred model (see Eq. 5 and Section 2.3.4). Annotations A, B, C & D correspond to the inferences shown in Fig. 4

domain to maximize information gain. However, as the dimensionality of the structure-property model increases, the curse of dimensionality makes it difficult to employ such a regular sampling strategy and in the 5DOF case, if bicrystals are employed exclusively, there will almost certainly be large gaps in the data resulting in the behavior exhibited in Fig. 4(a).

It is also noteworthy to compare Fig. 4(c) and (d). Both have a large number of observations ( $N_{\text{obs}} = 50$ ), but (c) is for bicrystals and (d) is for polycrystals with 100 grains. The bicrystal inference is notably more accurate and has a reduced uncertainty even though the polycrystals have a much more extensive sampling of the space (compare the associated histograms). We attribute this effect to the fact that as  $N_{\text{grains}}$  increases the sampling improves, but so does the number of degenerate configurations (i.e. the number of different structure-property models that could produce the same observed effective diffusivity). This suggests that if bicrystal data can be had in abundance, it will always be preferred—one would always choose abundant data with low uncertainty over abundant data with larger uncertainty. However, in many cases data is limited or costly and a trade-off must be made between data abundance and uncertainty, as will be discussed in more detail below.

It is interesting to note that in Fig. 5(a) the resolving power depends strongly on  $N_{\text{obs}}$ , but is almost completely independent of  $N_{\text{grains}}$ . This suggests that while the spatial distribution of what we learn is different for bicrystal and polycrystals, the *amount* that we learn is comparable.

One additional observation from Fig. 5(b) is that the accuracy of the inference appears to be much more sensitive to the quantity of data ( $N_{\text{obs}}$ ) than the type of data ( $N_{\text{grains}}$ ), and for a fixed value of  $N_{\text{obs}}$  inferences of comparable accuracy can be achieved over the entire range of  $N_{\text{grains}}$  that was tested.

While the tests we performed involved sets of microstructures having a uniform value of  $N_{\text{grains}}$ , the methods we have presented are in no way restricted to homogeneous data sets, but are perfectly capable of handling heterogeneous data sets composed of a mixture of bicrystals and polycrystals of any size or shape. Indeed we suggest that this is likely preferred to leverage the strengths of the different kinds of data: the polycrystals providing an inexpensive survey over the space and the bicrystals enhancing the resolution near GBs of interest (e.g. high-symmetry points in the space).

### 3.2. 3DOF Results

For the 3DOF inferences, we chose to visually represent the inference results over a mesh-based discretization of the Rodriguez space [40], with 43,914 tetrahedra and 8,406 vertices as shown in Fig. 6. In this context the model parameters to be inferred consisted of the logarithm of the function values at each of these 8,406 vertices:  $\mathbf{m} = \ln([\mathcal{D}(\omega_1), \mathcal{D}(\omega_2), \dots]^T)$ . Barycentric interpolation [41] (via Matlab’s `pointLocation()` function) was used to evaluate  $g(\mathbf{m}_k)$  in Eqs. 9 and 10 at each iteration.

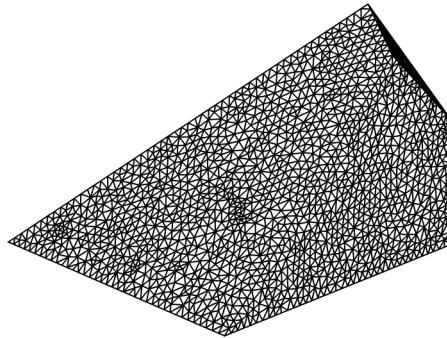


Figure 6: The cubic misorientation FZ discretized into 43,914 tetrahedra with 8,406 vertices for use in the 3DOF inferences.

We note that with 8,406 model parameters to infer, even when we consider 300 observations, the system is severely underdetermined and yet meaningful inferences can be made.

Three example inferences are shown in Fig. 7, including  $(N_{\text{grains}}, N_{\text{obs}}) = (2, 300), (10, 300), (100, 100)$ . As in the 1DOF tests, 10 inference replications were performed for each combination of  $N_{\text{obs}}$  and  $N_{\text{grains}}$ , and the results are presented in Fig. 8.

The trends in the 3DOF results are qualitatively similar to those from the 1DOF inferences, namely the strong dependence on  $N_{\text{obs}}$ , the weak dependence on  $N_{\text{grains}}$ , and the fact that uncertainty is larger in regions where observations are absent (note the bottom left edge of the bicrystal inference in Fig. 7(a)), which occur more often with bicrystal data.

There are also some notable differences between the 3DOF and 1DOF results. In the 3DOF case, more bicrystals are needed to achieve the same resolving power—for a resolving power of 0.8 about 70 bicrystal observations were needed in the 3DOF case, whereas only 7 were required in the 1DOF case—however, this represents a reduction in the number of observations required per dimension (compare  $70^{1/3} \approx 4$  for 3DOF to 7 for the 1DOF case). We attribute this to the spatial sharing of information: in 1D an observation can only affect the region to its left and right, whereas in 3D an observation provides information about a 3D neighborhood surrounding it so that more is learned per observation.

Comparing Fig. 5(b) and Fig. 8(b), it is also apparent that in the 3DOF case more observations are required to obtain the same level of accuracy as the 1DOF case. There is also a stronger dependence of the inference accuracy (MedAE) on  $N_{\text{grains}}$  in the 3DOF case. Moreover, the effect of  $N_{\text{grains}}$  appears to depend on the value of  $N_{\text{obs}}$ . For  $N_{\text{obs}} \lesssim 15$ , inference accuracy increases with  $N_{\text{grains}}$ , while for  $N_{\text{obs}} \gtrsim 15$  there is a modest decrease of accuracy with increasing  $N_{\text{grains}}$ .

Perhaps the most notable difference between the 3DOF results and the 1DOF results is the clear emergence of a transition between a data-sparse region where polycrystalline observations are preferred to the data-rich region where bicrystals are preferred. Figure 9 shows a set of slices through the contour plots of Figs. 5 and 8. For the 1DOF case the accuracy of the inferences is roughly the same for all  $N_{\text{grains}}$  below about  $N_{\text{obs}} = 5$ . For the 3DOF case, polycrystals with increasing  $N_{\text{grains}}$  outperform the bicrystals up to about  $N_{\text{obs}} = 20$ . As mentioned previously, when observations are abundant, direct bicrystal measurements are always preferred. However, it appears that there is a regime in which if the number of observations is sufficiently limited, polycrystalline samples will provide comparable accuracy or even outperform bicrystal data.

Moreover, the location of this transition varies with dimensionality. If we linearly extrapolate to the full 5DOF case, this would suggest that bicrystals would outperform polycrystals only when  $N_{\text{obs}} \gtrsim 35$ . On the other hand, bicrystals are typically more difficult and expensive to synthesize than polycrystals, so that when cost and efficiency are also considered the regime over which polycrystals are preferred may be considerably larger than simply the range of  $N_{\text{obs}}$  over which they outperform bicrystals for inference accuracy.

## 4. Conclusion

In this work we presented a method for inferring GB structure-property models from the effective properties of polycrystals or bicrystals with rigorously quantified uncertainty, when the number of measurements is smaller than the number of model parameters to be inferred (the underdetermined case). We performed validation tests for both 1DOF and 3DOF structure-property models for GB diffusivity in 2D (or columnar) microstructures.

We investigated the influence of the number of grains ( $N_{\text{grains}}$ ) in a polycrystal and the number of observations ( $N_{\text{obs}}$ ) on the quality of the inference. We found that inferences are far more sensitive to  $N_{\text{obs}}$  than  $N_{\text{grains}}$ , so that for a fixed value of  $N_{\text{obs}}$ , inferences of roughly equivalent resolving power can be obtained for microstructures over the entire range of  $N_{\text{grains}}$  that was investigated ( $[2, 100]$ ). For the 1DOF structure-property model, inference accuracy was also largely insensitive to  $N_{\text{grains}}$  over the tested

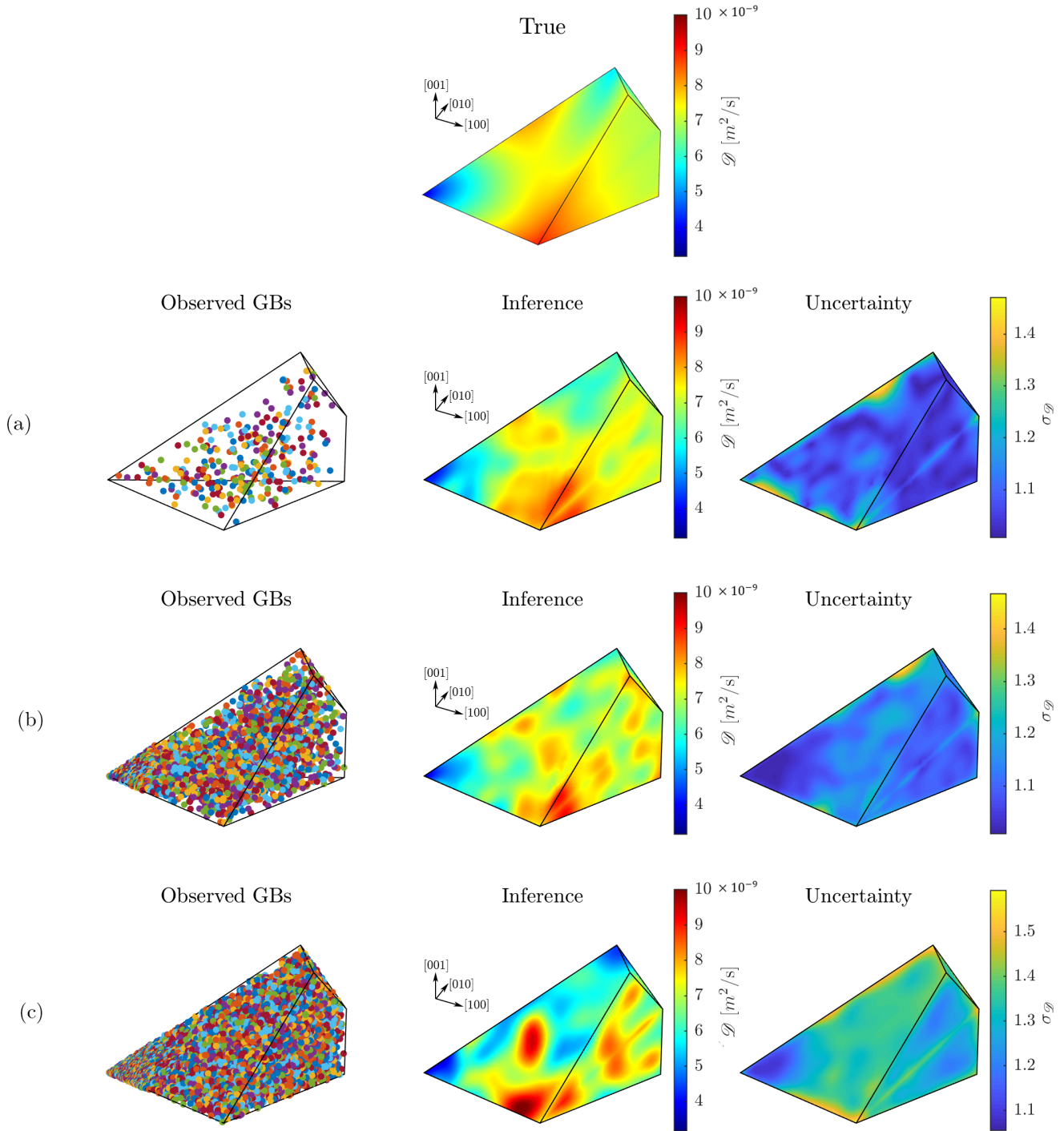


Figure 7: Three representative inferences corresponding to the points labeled A,B, & C in Fig. 8. In (a) 300 bicrystal observations were used, (b) is for 300 polycrystal observations with 10 grains each, and (c) shows the inference from 100 polycrystal observations with 100 grains each. From left-to right we show a scatter plot of GBs present in the set of observations, the resulting inference, and the posterior uncertainty. As a reminder, the uncertainty values are multiplicative ( $\mathcal{D} \ast \sigma_{\mathcal{D}}$ ), so they are unitless and a value of 1.0 would represent zero uncertainty. The true model is shown in Fig. 3.

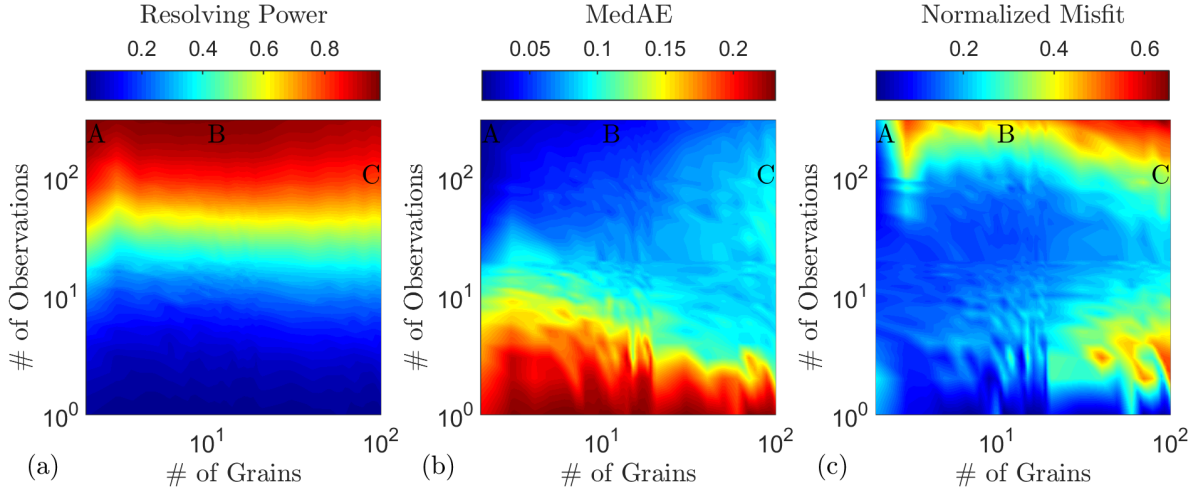


Figure 8: Contour plots of (a) resolving power (see Eq. 23), (b) median absolute error (see Eq. 24) between the inference and the true model, and (c) the normalized misfit of the inferred model (see Eq. 5 and Section 2.3.4). Annotations A, B, & C correspond to the inferences shown in Fig. 7.

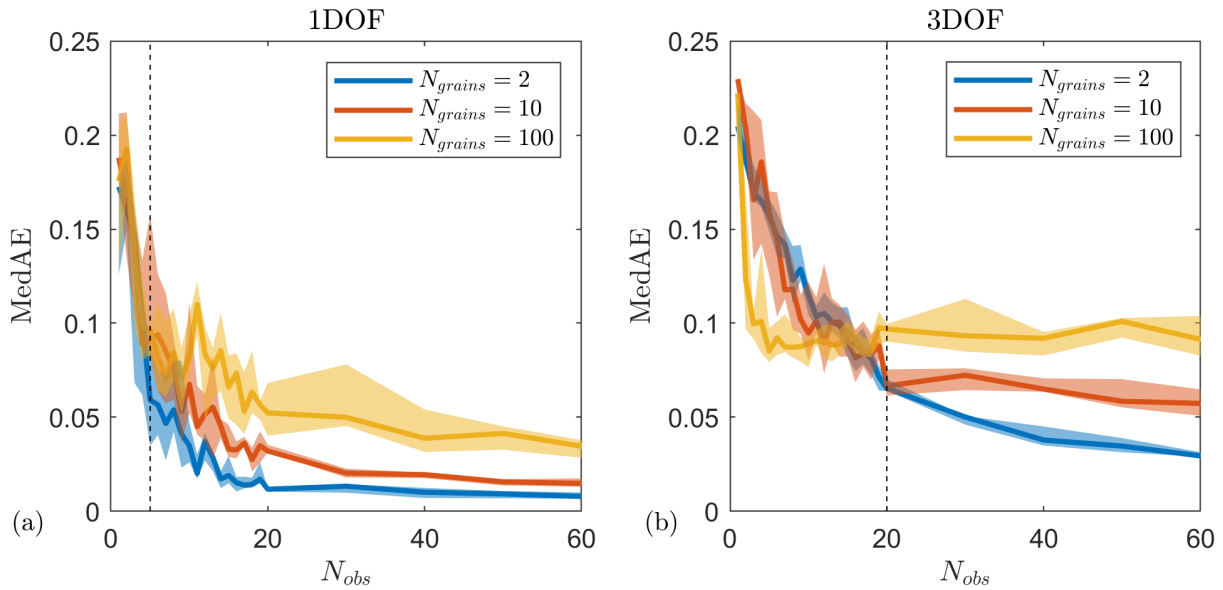


Figure 9: Median Absolute Error vs.  $N_{obs}$  for several values of  $N_{grains}$ , for both (a) 1DOF and (b) 3DOF inferences. Plots represent vertical slices through Fig. 5 and Fig. 8, respectively. Semitransparent envelopes represent the interquartile range of the data.

range. For the 3DOF structure-property model the effect of  $N_{\text{grains}}$  depends on  $N_{\text{obs}}$ . For  $N_{\text{obs}} \lesssim 15$ , inference accuracy increases with  $N_{\text{grains}}$ , while above  $N_{\text{obs}} \gtrsim 15$  there is a modest decrease of accuracy with increasing  $N_{\text{grains}}$ .

We also found that when observations are abundant, bicrystals produce inferences with greater accuracy (lower median absolute error). However, we observed a transition where at low values of  $N_{\text{obs}}$ , inferences with equivalent (1DOF) or greater (3DOF) accuracy were obtained with polycrystals. The location of this transition appears to increase with the dimensionality of the structure property model, such that for the full 5DOF case we anticipate that the data-limited regime where polycrystals are preferred for accuracy alone is likely to increase. Moreover, when additionally considering the reduced cost and complexity of synthesizing polycrystals, the regime over which polycrystals are preferred is likely to be much larger.

The results presented here employed 2D microstructures with diverse triple junction populations. While the methods presented apply to microstructures and structure-property models of arbitrary dimension, several factors may influence the sensitivity of the inferences to  $N_{\text{obs}}$  and/or  $N_{\text{grains}}$ , including: changes in the connectivity of GBs for 3D microstructures, and the degree of microstructural diversity available. These will be an important aspect to investigate in future work.

## Acknowledgement

The material presented here is based upon work supported by the National Science Foundation under Grant No. 1610077.

## References

- [1] D. L. Olmsted, E. A. Holm, S. M. Foiles, [Survey of computed grain boundary properties in face-centered cubic metals II: Grain boundary mobility](#), Acta Materialia 57 (13) (2009) 3704–3713. doi:[10.1016/j.actamat.2009.04.015](https://doi.org/10.1016/j.actamat.2009.04.015).
- [2] D. L. Olmsted, S. M. Foiles, E. A. Holm, [Survey of computed grain boundary properties in face-centered cubic metals: I. Grain boundary energy](#), Acta Materialia 57 (13) (2009) 3694–3703. doi:[10.1016/j.actamat.2009.04.007](https://doi.org/10.1016/j.actamat.2009.04.007).
- [3] R. C. Hugo, R. G. Hoagland, [The kinetics of gallium penetration into aluminum grain boundaries in situ TEM observations and atomistic models](#), Acta Materialia 48 (8) (2000) 1949–1957. doi:[10.1016/S1359-6454\(99\)00463-2](https://doi.org/10.1016/S1359-6454(99)00463-2).
- [4] J. Park, Y. Kim, J. An, F. Prinz, [Oxygen diffusion across the grain boundary in bicrystal yttria stabilized zirconia](#), Solid State Communications 152 (24) (2012) 2169–2171. doi:[10.1016/j.ssc.2012.09.019](https://doi.org/10.1016/j.ssc.2012.09.019).
- [5] F. Ye, C. Y. Yin, D. R. Ou, T. Mori, [Relationship between lattice mismatch and ionic conduction of grain boundary in ysz](#), Progress in Natural Science: Materials International 24 (1) (2014) 83 – 86. doi:<https://doi.org/10.1016/j.pnsc.2014.01.007>.
- [6] C. A. Fisher, H. Matsubara, [The influence of grain boundary misorientation on ionic conductivity in ysz](#), Journal of the European Ceramic Society 19 (6) (1999) 703 – 707. doi:[https://doi.org/10.1016/S0955-2219\(98\)00300-8](https://doi.org/10.1016/S0955-2219(98)00300-8).
- [7] I. Kaur, W. Gust, L. Kozma, [Handbook of grain and interphase boundary diffusion data](#), Ziegler Press, 1989.

- [8] T. Nakagawa, I. Sakaguchi, N. Shibata, K. Matsunaga, T. Yamamoto, H. Haneda, Y. Ikuhara, [Oxygen diffusion blocking of single grain boundary in yttria-doped zirconia bicrystals](#), *Journal of Materials Science* 40 (12) (2005) 3185–3190. doi:10.1007/s10853-005-2682-4.
- [9] A. K. Ivanov-Schitz, G. N. Mazo, [Atomistic Simulation of Interfaces in Materials of Solid State Ionics](#), *Crystallography Reports* 63 (1) (2018) 1–25. doi:10.1134/S106377451801008X.
- [10] G. Gottstein, D. A. Molodov, L. S. Shvindlerman, Grain boundary migration in metals: recent developments, *Interface Science* 6 (1-2) (1998) 7–22. doi:10.1023/a:1008641617937.
- [11] G. S. Rohrer, D. M. Saylor, B. El Dasher, B. L. Adams, A. D. Rollett, P. Wynblatt, The distribution of internal interfaces in polycrystals, *Zeitschrift fuer Metallkunde/Materials Research and Advanced Techniques* 95 (4) (2004) 197–214. doi:10.3139/146.017934.
- [12] S. Ratanaphan, D. L. Olmsted, V. V. Bulatov, E. A. Holm, A. D. Rollett, G. S. Rohrer, [Grain boundary energies in body-centered cubic metals](#), *Acta Materialia* 88 (2015) 346–354. doi:10.1016/j.actamat.2015.01.069.
- [13] V. V. Bulatov, B. W. Reed, M. Kumar, [Grain boundary energy function for fcc metals](#), *Acta Materialia* 65 (2014) 161–175. doi:10.1016/j.actamat.2013.10.057.
- [14] C. Kurniawan, S. Baird, D. T. Fullwood, E. R. Homer, O. K. Johnson, [Grain boundary structure-property model inference using polycrystals: the overdetermined case](#), *Journal of Materials Science* 55 (4) (2020) 1562–1576. doi:10.1007/s10853-019-04125-z.
- [15] J. Gottsmann, A. G. Camacho, J. Martí, L. Wooller, J. Fernández, A. García, H. Rymer, Shallow structure beneath the Central Volcanic Complex of Tenerife from new gravity data: Implications for its evolution and recent reactivation, *Physics of the Earth and Planetary Interiors* 168 (3-4) (2008) 212–230. doi:10.1016/j.pepi.2008.06.020.
- [16] B. Noetinger, V. Artus, G. Zargar, [The future of stochastic and upscaling methods in hydrogeology](#), *Hydrogeology Journal* 13 (1) (2005) 184–201. doi:10.1007/s10040-004-0427-0.
- [17] D. W. Vasco, K. Karasaki, K. Kishida, [A coupled inversion of pressure and surface displacement](#), *Water Resources Research* 37 (12) (2001) 3071–3089. doi:10.1029/2001WR000391.
- [18] R. F. Noriega, A. B. Ramirez, S. A. Abreo, G. R. Arce, [Implementation strategies of the seismic Full Waveform Inversion](#), in: 2017 IEEE International Conference on Acoustics, Speech and Signal Processing (ICASSP), IEEE, 2017, pp. 1567–1571. doi:10.1109/ICASSP.2017.7952420.
- [19] J. Shi, F. Faucher, M. V. De Hoop, H. Calandra, [Elastic full waveform inversion with surface and body waves](#), in: SEG Technical Program Expanded Abstracts, Vol. 35, Society of Exploration Geophysicists, 2016, pp. 1120–1124. doi:10.1190/segam2016-13961828.1.
- [20] A. Tarantola, *Inverse Problem Theory and Methods for Model Parameter Estimation*, Society for Industrial and Applied Mathematics, 2005. doi:10.1137/1.9780898717921.
- [21] K. Mosegaard, A. Tarantola, [Probabilistic approach to inverse problems](#), in: *International Geophysics*, Vol. 81 of *International Geophysics*, Elsevier, 2002, pp. 237–265. doi:10.1016/S0074-6142(02)80219-4.

- [22] A. Tarantola, K. Mosegaard, Mathematical basis for physical inference (2000). [arXiv:math-ph/0009029](https://arxiv.org/abs/math-ph/0009029).
- [23] K. Mosegaard, A. Tarantola, [Monte Carlo sampling of solutions to inverse problems](#), Journal of Geophysical Research: Solid Earth 100 (B7) (1995) 12431–12447. [doi:10.1029/94JB03097](https://doi.org/10.1029/94JB03097).
- [24] A. Tarantola, A. Nercessian, Threedimensional inversion without blocks, Geophysical Journal of the Royal Astronomical Society 76 (2) (1984) 299–306. [doi:10.1111/j.1365-246X.1984.tb05047.x](https://doi.org/10.1111/j.1365-246X.1984.tb05047.x).
- [25] A. Nercessian, A. Hirn, A. Tarantola, Threedimensional seismic transmission prospecting of the Mont Dore volcano, France, Geophysical Journal of the Royal Astronomical Society 76 (2) (1984) 307–315. [doi:10.1111/j.1365-246X.1984.tb05048.x](https://doi.org/10.1111/j.1365-246X.1984.tb05048.x).
- [26] A. Tarantola, B. Valette, Generalized nonlinear inverse problems solved using the least squares criterion, Reviews of Geophysics 20 (2) (1982) 219–232. [doi:10.1029/RG020i002p00219](https://doi.org/10.1029/RG020i002p00219).
- [27] C. A. Schuh, M. Kumar, W. E. King, [Analysis of grain boundary networks and their evolution during grain boundary engineering](#), Acta Materialia 51 (3) (2003) 687–700. [doi:10.1016/S1359-6454\(02\)00447-0](https://doi.org/10.1016/S1359-6454(02)00447-0).
- [28] M. E. Frary, C. A. Schuh, [Correlation-space description of the percolation transition in composite microstructures](#), Physical Review E - Statistical, Nonlinear, and Soft Matter Physics 76 (4) (2007). [doi:10.1103/PhysRevE.76.041108](https://doi.org/10.1103/PhysRevE.76.041108).
- [29] M. Kumar, W. E. King, A. J. Schwartz, [Modifications to the microstructural topology in f.c.c. materials through thermomechanical processing](#), Acta Materialia 48 (9) (2000) 2081–2091. [doi:http://dx.doi.org/10.1016/S1359-6454\(00\)00045-8](http://dx.doi.org/10.1016/S1359-6454(00)00045-8).
- [30] P. Davies, V. Randle, G. Watkins, H. Davies, [Triple junction distribution profiles as assessed by electron backscatter diffraction](#), Journal of Materials Science 37 (19) (2002) 4203–4209. [doi:10.1023/A:1020052306493](https://doi.org/10.1023/A:1020052306493).
- [31] M. E. Frary, C. A. Schuh, [Percolation and statistical properties of low- and high-angle interface networks in polycrystalline ensembles](#), Physical Review B 69 (13) (2004) 134115. [doi:10.1103/PhysRevB.69.134115](https://doi.org/10.1103/PhysRevB.69.134115).
- [32] T. R. Critchfield, O. K. Johnson, [Representative and statistical volume elements for grain boundary networks: A stereological approach](#) 188 (2020) 166–180. [doi:10.1016/j.actamat.2019.12.029](https://doi.org/10.1016/j.actamat.2019.12.029).
- [33] K. Smith, [On the Standard Deviations of Adjusted and Interpolated Values of an Observed Polynomial Function and its Constants and the Guidance they give Towards a Proper Choice of the Distribution of Observations](#), Biometrika 12 (1/2) (1918) 1. [doi:10.2307/2331929](https://doi.org/10.2307/2331929).
- [34] O. K. Johnson, J. M. Lund, T. R. Critchfield, [Spectral graph theory for characterization and homogenization of grain boundary networks](#), Acta Materialia 146 (2018) 42–54. [doi:10.1016/J.ACTAMAT.2017.11.054](https://doi.org/10.1016/J.ACTAMAT.2017.11.054).
- [35] L. G. Harrison, [Influence of dislocations on diffusion kinetics in solids with particular reference to the alkali halides](#), Transactions of the Faraday Society 57 (1961) 1191. [doi:10.1039/tf9615701191](https://doi.org/10.1039/tf9615701191).

- [36] S. Patala, C. Schuh, [Topology of homophase grain boundaries in two-dimensional crystals: The role of grain exchange symmetry](#), *Computers, Materials & Continua* 17 (2010) 1–18. doi:10.3970/cmc.2010.017.001.
- [37] J. B. Boisvert, C. V. Deutsch, [Programs for kriging and sequential Gaussian simulation with locally varying anisotropy using non-Euclidean distances](#), *Computers and Geosciences* 37 (4) (2011) 495–510. doi:10.1016/j.cageo.2010.03.021.
- [38] J. D’Errico, [nearestSPD](#) (2020).
- [39] N. J. Higham, [Computing a nearest symmetric positive semidefinite matrix](#), *Linear Algebra and its Applications* 103 (C) (1988) 103–118. doi:10.1016/0024-3795(88)90223-6.
- [40] P. Neumann, [Representation of Orientations of Symmetrical Objects by Rodrigues Vectors](#), *Textures and Microstructures* 14 (C) (1991) 53–58. doi:10.1155/tsm.14-18.53.
- [41] M. A. Ferdinand, *Der barycentrische Calcul, ein neues Hilfsmittel zur analytischen Behandlung der Geometrie*, Barth, 1827.